PAPER

On the conversion of CO_2 to value added products over composite PdZn and H-ZSM-5 catalysts: excess Zn over Pd, a compromise or a penalty?†

Christian Ahoba-Sam, [iD] [a] Elisa Borfecchia, [iD] [b] Andrea Lazzarini, [iD] [ac] Aram Bugaev, [iD] [de] Abdulrahman Adamu Isah, [f] Mostafa Taoufik, [f] Silvia Bordiga [iD] [ab] and Unni Olsbye [iD] *[a]

A challenge in converting CO_2 into hydrocarbons (HC) *via* methanol (MeOH) is the gap between the optimal temperature for each step (*i.e.* ≤250 °C for MeOH and ≥350 °C for HC). The focus of this study is to elucidate the cause of the limitations associated to oxygenate and hydrocarbon formation in combined PdZn and H-ZSM-5 catalysts at 250 to 350 °C. Starting with two different chemical states of Pd and Zn from two preparation approaches (physical mixture and surface organometallic chemistry grafting), *operando* X-ray absorption spectroscopy (XAS) and powder X-ray diffraction (PXRD) studies revealed similar PdZn alloy active phase formed during pretreatment in flowing H_2/Inert at 400 °C. The physical mixture performed better than the grafted analogue, with up to 8.8% yield to oxygenates (MeOH and dimethyl ether (DME); MeOH+) at 300 °C, close to the estimated thermodynamic yield (9.0%). The space–time yield (STY) of oxygenates increased from 250 to 300 °C, reaching 8.5 $mol_{(MeOH+)}$ $kg_{(PdZn)}^{-1}$ h^{-1}. The catalyst performance surpassed other reported yields in similar systems, which activity declined with temperature even below 300 °C. Operando XAS and PXRD experiments further showed that the PdZn phase active for MeOH formation was maintained during testing in the 250–350 °C range. InfraRed (FT-IR) and XAS experiments revealed the poisoning of Brønsted acid sites in H-ZSM-5 by Zn(II) exchange, thereby rendering it inactive for hydrocarbon formation. Overall, to avoid biasing the hybrid catalyst performance, a careful and balanced choice of the compositional characteristics will be crucial in designing an improved multi-functional catalytic system for CO_2 valorisation.

1. Introduction

Chemical conversion of CO_2 to value-added chemicals and fuels potentially presents an important substitute for the rapidly dwindling and non-renewable fossil fuels that are currently the major source of chemicals and energy in the

world.[1–3] Some key reactions in CO_2 hydrogenation are illustrated in eqn (1)–(4). As illustrated in Fig. 1, the highly exothermic methanol (MeOH), dimethyl ether (DME) or
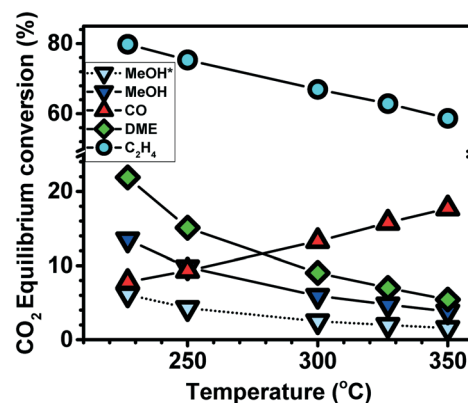
[a] *SMN Centre for Materials Science and Nanotechnology, Department of Chemistry, University of Oslo, N-0315 Oslo, Norway. E-mail: unni.olsbye@kjemi.uio.no*

[b] *Department of Chemistry, NIS Center and INSTM Reference Center, University of Turin, 10125, Turin, Italy*

[c] *Department of Physical and Chemical Sciences, University of l'Aquila, Via Vetoio 42 (COPPITO 2), 67100, l'Aquila, Italy*

[d] *The Smart Materials Research Institute, Southern Federal University, Sladkova 178/24, 344090, Rostov-on-Don, Russia*

[e] *Southern Scientific Centre, Russian Academy of Sciences, Chekhova 41, 344006 Rostov-on-Don, Russia*

[f] *Université Lyon 1, Institut de Chimie Lyon, CPE Lyon CNRS, UMR 5265 C2P2, LCOMS, 43 Bd du 11 November 1918, 69616 Villeurbanne Cedex, France*

† Electronic supplementary information (ESI) available: N_2 adsorption, TEM, XAS, PXRD, test results. See DOI: 10.1039/d0cy00440e

Fig. 1 CO_2 equilibrium conversion at 20 bar (*8 bar) *versus* temperature, following eqn (1)–(4).

This journal is © The Royal Society of Chemistry 2020

Catal. Sci. Technol., 2020, **10**, 4373–4385 | **4373**

hydrocarbons formation are thermodynamically favoured at low temperature while the contrary is true for the endothermic reverse water shift reaction (RWGS, eqn (2)). Hence, MeOH synthesis is often carried out at relatively low temperature and high pressure.[4] Currently, MeOH is commercially produced from synthesis gas (mainly CO and H_2) over ICI developed $Cu/ZnO/Al_2O_3$ catalyst at 50–100 bar and 200–300 °C.[5] However, when the feed consists of CO_2 and H_2, the RWGS reaction is highly enhanced over the $Cu/ZnO/Al_2O_3$ catalyst, leading to substantial selectivity loss.[6] Recently, several metals and metal oxides have been reported to be active for CO_2 hydrogenation to MeOH, including Pd-based,[6–16] In-based,[17–22] and Zn/ZrO_2-based[23–29] catalysts.

Reaction	$\Delta H_{298} \left(\frac{kJ}{mol}\right)$	$\Delta G_{298} \left(\frac{kJ}{mol}\right)$	Eqn
$CO_2 + 3H_2 \rightleftharpoons CH_3OH + H_2O$	−49.2	3.7	(1)
$CO_2 + H_2 \rightleftharpoons CO + H_2O$	41.2	28.8	(2)
$CO_2 + 3H_2 \rightleftharpoons 0.5CH_3OCH_3 + 1.5H_2O$	−61.2	−5.7	(3)
$CO_2 + 3H_2 \rightleftharpoons 0.5CH_2CH_2 + 2H_2O$	−63.9	−29.2	(4)

Among them, PdZn-based catalysts have shown promising MeOH yield especially at medium temperatures (210–270 °C).[6–9,11,30] By applying different catalyst preparation methods, Bahruji et al.[7,8] reported that increasing the Zn/Pd ratio led to increased Zn^0 incorporation in Pd lattice, enhancing surface PdZn alloy formation and increasing MeOH production. However, when only Pd without Zn was deposited on TiO_2 or Al_2O_3, CO was predominantly produced suggesting that pure Pd sites promote RWGS reaction while the presence of Zn is crucial to MeOH production.[6,10,30] By introducing a CdSe shell around a Pd–Zn core, a study by Liao et al.[6,30] indicated that deeper reduction of Zn^{II} to Zn^0 could be attained at milder temperatures (280 °C) which subsequently enhanced the number of neighbouring Zn^0 around the Pd^0 atoms leading to 80–90% MeOH selectivity at 270 °C. A mechanistic study using DRIFT and DFT calculations suggested that, possible intermediates in CO_2 hydrogenation over PdZn catalysts could be either (i) HCOO which directly hydrogenates to MeOH or (ii) trans-COOH, which isomerize to cis-COOH for RWGS route or MeOH.[6,9] trans-COOH formation was found to be energetically favoured on pure Pd (111) while it was highly unstable on Pd_1Zn_1 (111). The authors concluded that, the PdZn site on the catalyst surface suppresses trans-COOH formation, thereby suppressing the RWGS reaction. Hence, increasing amounts of Zn minimized isolated Pd, thereby suppressing RWGS reaction and promoting MeOH formation.

Beyond the possible improvements of PdZn-based catalysts, MeOH production is still limited by thermodynamic equilibrium, especially at increasing temperatures (>200 °C). Here, instead, CO formation is thermodynamically favoured, leading to decreasing MeOH selectivity with increasing temperature. Literature examples of this effect are shown in Fig. 2 for PdZn-based catalysts. In addition to the decreasing MeOH selectivity, MeOH productivity numbers were also reported to decrease with increasing temperature for the Pd:Zn/TiO_2 catalyst, already between 210–250 °C. For the other
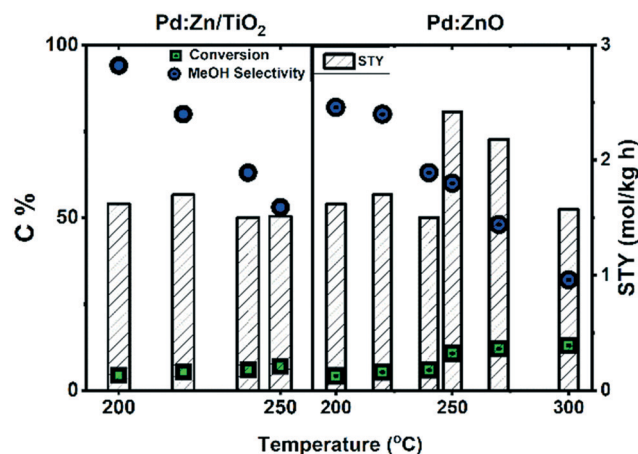

Fig. 2 CO_2 conversion (box), MeOH selectivity (circle) and MeOH space–time yield (STY, bars) versus temperature over two Pd:Zn catalysts, Pd:Zn/TiO_2 (left) and Pd:ZnO (right). Adapted from[7,8]

catalyst, Pd:ZnO, MeOH production was reported to decrease at temperatures beyond 250 °C.[7,8]

The dehydration of formed MeOH to dimethyl ether (DME) presents one means by which the reaction selectivity can be shifted away from CO at temperatures beyond 250 °C. Beside being a thermodynamic driving force (see Fig. 1), DME can be used directly as an environmentally friendly fuel or as a key feedstock in the methanol-to-hydrocarbons (MTH) reaction over zeolites.[31–33] To convert CO_2 to DME, there is a need for a bi-functional catalyst composed of MeOH catalyst and an acidic catalyst for dehydration. Reported, solid acid catalysts used for such reactions in combination with MeOH synthesis catalysts include sulphated ZrO_2,[34] alumina[35,36] and zeolites.[36–38] Among them, combination of MeOH based catalyst and zeolite has shown promising DME production within 220–330 °C.[36,38] One drawback is that adsorbed water during the reaction can induce sintering of MeOH synthesis catalyst.[38] This implies that, since water is a major product in the CO_2 to DME reaction, a hydrophobic catalyst with optimum acidity is preferred. Increasing the Si/Al ratio has been reported to decrease the hydrophilicity of H-ZSM-5 zeolite significantly.[39] Aside the acid sites density, the strength of the acid sites, the pore size, the micro and meso porosity of the solid acid also play an important role in MeOH dehydration.[40] Even though both Lewis acid and Brønsted acid sites are known to aid in dehydration, Brønsted acid sites are more favourable.[41] However, the stronger the acid strength, the more they promote coking to deactivate the catalyst.[40]

The method for mixing the two catalytic functions is important to obtain an optimal interaction between the active sites for MeOH synthesis and dehydration, respectively, avoiding their mutual poisoning or restricting MeOH diffusion. Prior studies have shown that composite physical mixture of PdZn alloy and H-ZSM-5 produces higher amount of oxygenates across 220 to 300 °C, compared to a chemical vapour impregnated H-ZSM-5 with PdZn.[36] N_2

4374 | Catal. Sci. Technol., 2020, **10**, 4373–4385

This journal is © The Royal Society of Chemistry 2020

physisorption and NH_3 TPD of the H-ZSM-5 before and after impregnation showed a decrease in the accessible surface area and a clear decrease in the number of strong acid sites while the weak acid sites were preserved after impregnation. This result was attributed to blocking of the zeolite micropores by PdZn nanoparticles which restricted MeOH access to such sites. They further implied that, while the two catalysts need to be in close proximity to each other, there was no apparent MeOH diffusion restriction from the MeOH catalyst to the zeolite surface for the physically mixed hybrid catalyst.

The conversion of CO_2 and H_2 to hydrocarbons *via* MeOH would enable substantially higher per pass yields than the conversion to MeOH or DME (see Fig. 1). A general challenge of this process is the gap between the optimal temperature for each step. As described above,[1,42] CO_2 hydrogenation to MeOH or DME is favoured by low temperature and high pressure while MeOH or DME to hydrocarbons – a reaction that is catalysed by Brønsted acidic zeolites - is favoured by temperatures above 350 °C.[43,44]

In the present study, our aim is to elucidate the cause of the previously reported limitations associated to oxygenate and hydrocarbon formation in the combined PdZn and H-ZSM-5 catalyst system at 270 to 350 °C. To this aim, we have studied PdZn@ZnO alone and physically mixed with H-ZSM-5 as well as PdZn chemically grafted on H-ZSM-5 through surface organometallic chemistry (SOMC), for the CO_2 hydrogenation reaction at 250 to 350 °C. The latter methodology (SOMC) offers a controlled environment of the bi-metallic nanoparticles.[45] Cardinal in the current work was the use of combined *operando* X-ray absorption spectroscopy (XAS) and powder X-ray diffraction (PXRD) to study the hybrid catalyst stability at relatively high pressures conditions (8 bar). This study also addresses the penalty involved in having excess Zn in the PdZn mixed with H-ZSM-5 zeolite as a bi-functional catalyst in one bed.

2. Experimental

2.1 Catalyst preparation

Commercial ZSM-5 CBV-5524 G (Si/Al = 25) and CBV 8014 (Si/Al = 40) were purchased from Zeolyst International. The parent ZSM-5 was ion exchanged with 1 M NH_4NO_3 solution twice for 2 h each at 70 °C over water bath. The resulting mixture was centrifuged, oven dried and then calcined at 550 °C for 2 h to obtain H-ZSM-5. PdZn @ZSM-5 was prepared by grafting $Pd(acac)_2$ in dry toluene on *meso*-H-ZSM-5 (obtained after desilication described elsewhere[46]) using SOMC (surface organometallic chemistry) on oxide followed by reduction under H_2 at 500 °C (4 h) to achieve supported Pd metal particles. This procedure was followed by a second grafting, using SOMC diethylzinc in dry toluene on metal (Pd particles) and then further reduction in H_2 at 500 °C (4 h) to give the bimetallic PdZn on H-ZSM-5 named PdZn@H-ZSM-5.[45] PdZn@ZnO was prepared by incipient impregnation of ZnO powder with $Pd(NO_3)_2$ (both purchased from Sigma-Aldrich)

following similar route as reported by Tew *et al.*[47] 0.8 g $Pd(NO_3)_2 \cdot 6H_2O$ was dissolved in 1 ml water and thoroughly mixed with 3 g of ZnO powder to form a thick paste. The paste was dried at 80 °C overnight, and then calcined at 500 °C under static air for 3 h. The resulting material was reduced under H_2 at 400 °C for 1 h to form the PdZn@ZnO sample. The PdZn@ZnO was physically mixed with H-ZSM-5 for the CO_2 hydrogenation reaction.

2.2 Catalyst characterization

BET surface area & electron microscopy. The surface area and micropore volume were determined from N_2 physisorption using BEL BELSORP-mini II instrument at −196 °C. About 50 mg samples were preheated under vacuum at 80 °C °C for 1 h and 300 °C for 2 h to remove moisture and any other adsorbate before adsorption measurement. The specific surface area was estimated using BET equation at pressure range between 0 to 0.2 relative to the saturated vapour pressure (101 kPa). SEM images as well as the EDS elemental composition of the samples were taken on a Hitachi SU8230 field emission scanning electron microscope (FE-SEM). The TEM imaging and EDS analysis was done with Jeol 2100F instrument. Samples were diluted in absolute ethanol and separated in an ultrasound bath for 30 min. This was then dropped on carbon film on a Cu grid.

Lewis and Brønsted acidity probed by FT-IR spectroscopy of adsorbed pyridine. The experimental procedure employed can be found in ref. 48. Spectra were collected by means of a Bruker Vertex80 instrument equipped with a liquid nitrogen-cooled MCT detector. Each spectrum was obtained by averaging 64 acquisitions with a spectral resolution of 2 cm^{-1}. Each sample was pressed without any dilution into a self-sustained pellet and placed inside a gold envelope sample holder. Subsequently, the pellet was transferred to a dedicated cell, designed to perform both catalyst activation and spectroscopic measurements, being equipped with KBr windows. Before pyridine adsorption, samples were treated at 400 °C in dynamic vacuum for 3 h, then they were cooled to room temperature and ~20 mbar of pyridine were dosed and left to equilibrate for 30 min. Since we are interested only in the pyridine chemisorbed on the acid sites of the catalyst, the samples were outgassed first 30 min at room temperature and then at 200 °C for 2 h, in order to remove excess and physisorbed pyridine. In case of PdZn@ZnO + H-ZSM-5 sample, in addition to the standard treatment used to remove adsorbed water and other impurities (400 °C in dynamic vacuum for 3 h), a further stage of treatment in H_2 at 400 °C was adopted to clarify the behaviour of Zn having the co-presence of the zeolite and hydrogen. Brønsted and Lewis sites were quantified based on the integrated intensity of the bands at 1544 and 1455 cm^{-1} respectively, using the integrated molar extinction coefficient reported in previous literature.[49] In order to overcome the sample thickness issue and making different samples comparable, the mass of the zeolitic phase of each pellet was measured using a Denver

This journal is © The Royal Society of Chemistry 2020

Catal. Sci. Technol., 2020, **10**, 4373–4385 | **4375**

Instrument SI-234 analytical balance and its surface was measured by means of a Leica DFC425 optical microscope. Moreover, in case of the physical mixture, the integrated intensities of the bands have been considered evaluating the fraction of zeolite in respect to the total amount of sample. In this way, it is possible to rank the amount of acid sites, by normalizing the area of the peaks corresponding to Brønsted and Lewis sites to the surface density of the samples.

***Operando* XAS and PXRD.** *Operando* XAS and PXRD experiments were performed at the BM31 beamline (Swiss Norwegian Beamline, SNBL) of the European Synchrotron Radiation Facility (ESRF, Grenoble, France).[50] For the measurements, PdZn@H-ZSM-5 and PdZn@ZnO + H-ZSM-5 (physical mixture, PdZn@ZnO : H-ZSM-5 = 1:3 by weight) were carefully ground and sieved with 250 to 177 μm sieves. For Pd K-edge measurements, *ca.* 10 mg of powder were packed in a 2.5 mm-diameter capillary, while for Zn K-edge data collection, *ca.* 1 mg of catalyst was packed in a 0.7 mm-diameter capillary. The capillary reactor was then connected to an appropriate gas-flow setup for the CO_2 hydrogenation reaction. Temperature at the measurement position was controlled by a heat gun. A total flow rate of 12 ml min^{-1} was employed during all the experiments, consisting of i) activation from ambient temperature to 400 °C at 1 bar in $10H_2/2He$ and kept for 60 min at 400 °C, ii) cooling down to 250 °C in H_2 and flushing with He, iii) pressurizing in He to 8 bar iv) CO_2 hydrogenation reaction with $2.5CO_2/7.5H_2/2He$ at 250, 300, 350 °C at 60 min reaction time for each temperature.

Pd K-edge and Zn K-edge XAS spectra were collected in transmission mode, using a water-cooled flat Si(111) double-crystal monochromator. To measure the incident (I_0) and transmitted (I_1) X-ray intensity, 30 cm-length ionization chambers filled with a mixture of He and Ar were used. We characterized static states for each catalyst collecting two consecutive XAS scans, of *ca.* 10 min each, in the energy ranges 24 100–25 300 eV and 9400–10 500 eV, for Pd K-edge and Zn K-edge, respectively, with constant energy step of 0.4 eV in the continuous scanning mode. Shorter XAS scans, of *ca.* 2 min per scan were employed to monitor the evolution of the spectroscopic features during the activation ramp in H_2. Pd and Zn foils were measured simultaneously using a third ionization chamber for energy calibration.

XAS spectra were normalized to unity edge jump using the Athena software from the Demeter package.[51] Extraction of the $\chi(k)$ EXAFS functions and Fourier transforms were also performed using Athena program.

PXRD data were collected quasi-simultaneously with XAS measurements. The patterns were recorded by CMOS-Dexela 2D detector. The sample-to-detector distance l = 419.91(8) mm and photon wavelength λ = 0.50544(2) Å, selected by a Si(111) channel-cut monochromator, were calibrated using reference LaB_6 and Si materials. The above geometry resulted in 2θ range 1.2–35.0 (d_{min} = 0.85 Å). For a given experimental condition, 5 consecutive acquisition by 10 s each were acquired and averaged. For dark field correction, dark images

(with closed X-ray shutter) were collected with the same statistics and subtracted from the data. Azimuthal integration of 2D patterns was done in PyFAI code[52] to obtain $I(2\theta)$ data using integration parameters initially determined in Fit2D program.[53]

2.3 Catalytic tests

Catalytic tests were performed in a fixed bed continuous flow stainless steel reactor (I.D. 8.3 mm). 150–300 mg pelleted catalyst in the range of 240–420 μm grain size was loaded in the reactor and pre-treated *in situ* at 400 °C for 1 h at 1 atm in a flow of H_2 gas (10 ml min^{-1}) before cooling to reaction temperatures. All quoted flows are at STP. The total pressure was then increased in He to 20 bar controlled by a back-pressure regulator (Bronkhorst P-702CV). The reactant gas mixture ($1CO_2 : 3H_2 : 1(10\%$ Ne in He)) was then introduced in the reactor system. A standard total gas flow rate was kept at 30 ml/min with mainly GHSV of 6000 ml g_{cat}^{-1} h^{-1}. In the case of testing only PdZn@ZnO without zeolite, 50% SiO_2 was added. The post-reactor lines were heated at about 200 °C to avoid product condensation. The effluent was analysed using an online Agilent 7890B GC and Agilent 3000 micro-GC connected to FID and TCD respectively. CO_2 conversion and product selectivity were calculated using the formulas below:

$$\text{Conversion}, X_{CO_2} = \frac{\text{Total number of C in all products}}{\text{Total number of C in all effluent}} \times 100$$

$$\text{Selectivity}_{\text{product}_A} = \frac{\text{Total number of C in product}_A}{\text{Total number of C in all products}} \times 100$$

Space time yield of A

$$= \frac{\text{Volume}_{CO_2,\text{in}} \times X_{CO_2} \times \text{Selectivity}_A \times 60}{24500 \times \text{mass of PdZn catalyst}} \left(\frac{\text{mol}}{\text{g·h}}\right)$$

Since the PdZn alloy is generally accepted to be the active site for the formation of MeOH,[6,30] the mass of the active component for MeOH was estimated based on the Pd and Zn mass.

3. Results

3.1 BET and electron microscopy

The Si/Al ratio of the parent H-ZSM-5 used in the study were 25 and 40, hereafter the samples are named "H-ZSM-5 (25)" and "H-ZSM-5 (40)" respectively. Despite the difference in the Si/Al of the H-ZSM-5 zeolites, their specific surface area and particle sizes were very similar (see Table 1 and Fig. 3). The BET surface areas were 444 and 420 m^2 g^{-1} while the micropore volumes were 0.196 and 0.176 cm^3 g^{-1} for the H-ZSM-5 (40) and H-ZSM-5 (25), respectively (see also ESI,† Fig. S1 for the adsorption isotherms). The H-ZSM-5 (25) was used for the PdZn grafting while the H-ZSM-5 (40) was used for the physical mixing with PdZn@ZnO. Upon grafting the PdZn on

4376 | *Catal. Sci. Technol.*, 2020, **10**, 4373–4385

This journal is © The Royal Society of Chemistry 2020

Table 1 Chemical composition and textural properties of the catalyst samples

Sample	Elemental composition		Textural properties	
	Si/Al	Zn/Pd	BET area (m^2 g^{-1})	Micropore volume (cm^3 g^{-1})
H-ZSM-5 (25)	25		420	0.176
PdZn@H-ZSM-5 (25)	25	5	348	0.121
H-ZSM-5 (40)	40		444	0.196
PdZn@ZnO		16		

H-ZSM-5 (25), the BET surface area was 348 m^2 g^{-1} while micropore volume also reduced to 0.121 cm^3 g^{-1}. The PdZn grafted on H-ZSM-5 (25) was named PdZn@H-ZSM-5 (25), and contained 1.5 wt% Pd. The TEM imaging (of the as-prepared PdZn@H-ZSM-5 (25), Fig. 3c) showed spherical metal or alloy (PdZn) nanoparticles (NPs) of predominantly 9 ± 3 nm (see ESI† Fig. S3 for particle distribution curve), with the smaller NPs grafted within the zeolite while larger NPs were observed at the edges. The Pd impregnated ZnO was named PdZn@ZnO, as H_2 reduction pre-treatment is expected to give PdZn alloy, over ZnO support (more details will follow in section 3.3). The Pd loading in the PdZn@ZnO was 3.3 wt%. TEM imaging of the H_2 reduced (pre-treated) impregnated sample (Fig. 3d) also showed spherical but larger metal/alloy particles of about 13 ± 7 nm size on top of ZnO particles (identified from EDS spot analysis, see ESI† Fig. S2).

3.2 Pyridine adsorption FT-IR spectroscopy

Basic probe molecules coupled with FT-IR spectroscopy are one of the easiest and most used tools for acid sites characterization in solid state samples. Among all the possible alternatives, pyridine allows to perform a quantitative analysis of the different acid sites distinguishing Brønsted from Lewis sites, with methods well described in the specialized literature.[48,49] The spectral region of interest is the one between 1600 and 1400 cm^{-1}, where we observe two specific bands unequivocally ascribable to the pyridinium ion, originated through the interaction of pyridine with strong Brønsted acidic sites (1544 cm^{-1}) and to strongly adsorbed pyridine on Lewis sites, associated to extra-lattice Al^{3+} and Zn^{2+} (1455 cm^{-1}).

Part (a) of Fig. 4 illustrates the data associated to the sample H-ZSM-5 (25), while part (b) refers to H-ZSM-5 (40). From the two set of data it is evident that the preparation method of the two samples affects substantially the number and the type of the acidic sites. Black curves in part (a) and (b) show that the starting points (protonic parent zeolites) are very similar, presenting a majority of Brønsted acidic sites and a minor number of Lewis species ascribable to few extra-lattice Al^{3+} species. In case of the sample in which PdZn nanoparticles were obtained by direct deposition on the parent zeolite (orange curve in part (a) of Fig. 4), major changes occur already in the "as-prepared" sample, as evidenced by the major decrease of the band associated to the pyridinium and the substantial growth of the band ascribed to pyridine adsorbed on Lewis sites (most probably Zn^{2+}). Conversely, the spectrum obtained after catalyst use
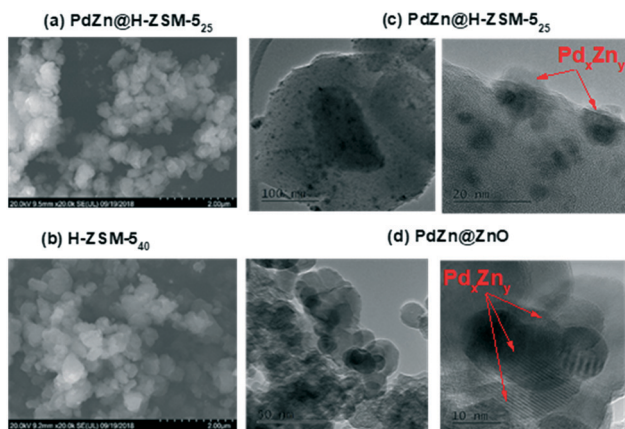

Fig. 3 SEM (a) and (b) and TEM (c) and (d) of the catalyst samples investigated. The PdZn@H-ZSM-5 sample was reduced in H_2 at 500 °C for 4 h, and the PdZn@ZnO sample was pretreated in H_2 at 400 °C for 1 h, prior to the investigation. The Pd_xZn_y phases were determined using d-spacing values from the HRTEM see details in the ESI† Fig. S2.
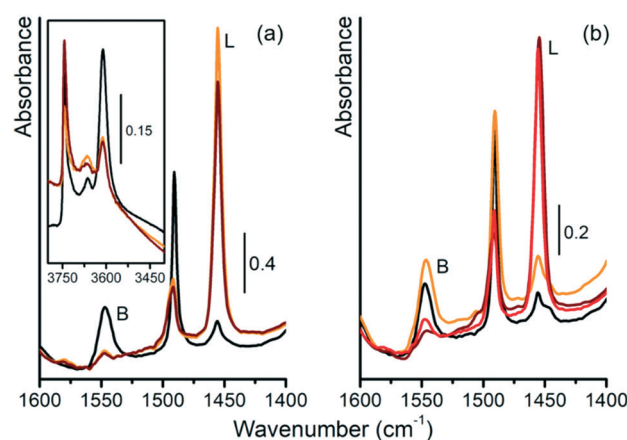

Fig. 4 FT-IR spectra highlighting the bands of pyridinium originated from the strong Brønsted (B) acid sites and of pyridine adsorbed on Lewis (L) sites. Part (a): Black curve represents the parent H-ZSM-5(25), orange curve represents the PdZn@H-ZSM-5(25) as-prepared sample, brown curve represents the PdZn@H-ZSM-5(25) tested sample. Inset shows a magnification of the ν(OH) region for the same samples prior to pyridine dosing. Part (b): Black curve represents the parent H-ZSM-5(40), orange curve represents the PdZn@ZnO + H-ZSM-5(40) as-prepared sample, red represents PdZn@ZnO + H-ZSM-5(40) sample treated with H_2 at 400 °C for 1 h; brown curve represents the PdZn@ZnO + H-ZSM-5(40) tested sample.

This journal is © The Royal Society of Chemistry 2020

Catal. Sci. Technol., 2020, **10**, 4373–4385 | **4377**

(brown curve in part (a) of Fig. 4) does not show major changes in the number of Brønsted and Lewis acid sites apart from a small decrease (about 10%) of the latter that can be interpreted by considering that some of them are not accessible anymore to the probe. Moving to the sample obtained by physical mixture of PdZn@ZnO and H-ZSM-5 (40), (orange curve in part (b) of Fig. 4), it is clear that no significant changes are observed in the "as-prepared" sample, with respect to the respective abundance of Brønsted and Lewis acidic sites. Conversely, once the sample has been treated in H_2 at 400 °C for 1 h (red curve in part (b) of Fig. 4), major decrease of the band associated to the pyridinium and the substantial growth of the band ascribed to pyridine adsorbed on Lewis sites (most probably Zn^{2+}) occur, testifying a migration of metal ions that substitute acidic protons in the zeolitic framework. Conversely, the spectrum obtained after the catalyst use (brown curve in part (b) of Fig. 4) does not show major changes in the number of Brønsted and Lewis acidic sites. The inset of Fig. 4(a), illustrates the zeolite spectra in the ν(OH) region showing the substantial decrease of the band at 3610 cm^{-1}, occurring upon the PdZn functionalization. The quantification of Brønsted and Lewis sites are reported in Table 2. Thanks to the full set of data, it is clear that zinc has a high affinity towards the acidic zeolites easily replacing the protons, implying a substantial decrease of the Brønsted acidity in favour of the introduction of Lewis sites.

3.3 *Operando* XAS and PXRD studies

To obtain detailed information on the electronic and structural properties of the investigated PdZn-zeolite bifunctional catalysts, we combined XAS and PXRD measurements at the BM31 beamline of the ESRF. We firstly considered the activation process, carried out in H_2 from RT to 400 °C, comparing the time-dependent evolution of Pd and Zn K-edge XAS data for both PdZn@H-ZSM-5 (25) and PdZn@ZnO + H-ZSM-5 (40). Fig. 5 reports an overview of the results, together with reference spectra for selected model compounds at both absorption edges, to guide the data interpretation.

Considering Pd K-edge spectra in Fig. 5a and c, we note how the initial state at 50 °C in He, prior to activation in H_2, differs for the two catalysts. PdZn@H-ZSM-5 (25) already shows the characteristic features of Pd^0. Conversely, for the

PdZn@ZnO + H-ZSM-5 (40) physical mixture, a substantial fraction of Pd is still in the Pd^{II} oxidation state, with an energy position of the edge compatible with that of the PdO model compound. Switching the gas feed to pure H_2, Pd efficiently undergoes reduction to Pd^0 also in the PdZn@ZnO + H-ZSM-5 (40) catalyst, as clearly evidenced by the shift of the edge position to lower energy values. Comparison with the XANES and FT-EXAFS spectra of bulk Pd metal in Fig. 5e points to the presence of Pd metal nanoparticles in both the materials. As temperature increases during activation, the position of the edge remains unchanged, supporting a stable Pd^0 oxidation state. Nonetheless, from *ca.* 300 °C upward, the spectral features further evolve showing very similar modifications for the two investigated catalysts, albeit occurring at slightly lower temperature for PdZn@H-ZSM-5 (25) with respect to PdZn@ZnO + H-ZSM-5 (40). In particular, the XANES post-edge oscillations characteristic of metal Pd become progressively flatter and, at the end of the activation, a XANES line-shape significantly different from the one of metal Pd is observed. In parallel, the FT-EXAFS restructures towards a broad single maximum, peaking at *ca.* 2.15 Å in the (phase-uncorrected) spectra of both catalysts. Based on the previous literature[47,54,55] and in agreement with the PXRD results presented below, these XAS fingerprints are diagnostic for the formation of a PdZn nano-alloy, representing the active phase for CO_2 hydrogenation over both bi-functional catalysts. According to previous reports, the broad peak in the FT-EXAFS stems from the combination in partial antiphase of Pd–Zn and Pd–Pd scattering contributions, expected at 2.64 Å and 2.90 Å, respectively, for the tetragonal $L1_0$ structure of the PdZn alloy.[47,55] According to further analysis of FT-EXAFS analysis (See ESI,† Fig. S5 and S6), only minor fraction of pure Pd nanoparticles remains after the activation, which further converts completely to a Pd–Zn alloy under reaction conditions.

In parallel, Zn K-edge XAS measurements allowed us to characterize the average properties of Zn-species in the bi-functional catalysts, keeping in mind that Zn is present in excess with respect to Pd in both cases (see Table 1). In contrast to Pd K-edge results, pointing to a very similar local structure around Pd sites in both the activated materials, Zn K-edge XAS shows markedly different trends for PdZn@H-ZSM-5 (25) and PdZn@ZnO + H-ZSM-5 (40). In particular, for PdZn@H-ZSM-5 (25) (see Fig. 5b), the evolution during activation closely resembles what has been previously reported for Zn-exchanged

Table 2 Summary of the acid sites quantification using pyridine FT-IR spectroscopy

Sample	Step	Brønsted sites (mmol g^{-1})	Lewis sites (mmol g^{-1})
Fresh H-ZSM-5	Si/Al = 25	0.21	0.07
	Si/Al = 40	0.15	0.07
PdZn@H-ZSM-5 (25)	As prepared	0.02	0.57
	Tested	0.02	0.46
PdZn@ZnO + H-ZSM-5 (40)	As prepared	0.11	0.05
	Activated	0.04	0.25
	Tested	0.03	0.32

4378 | *Catal. Sci. Technol.*, 2020, **10**, 4373–4385

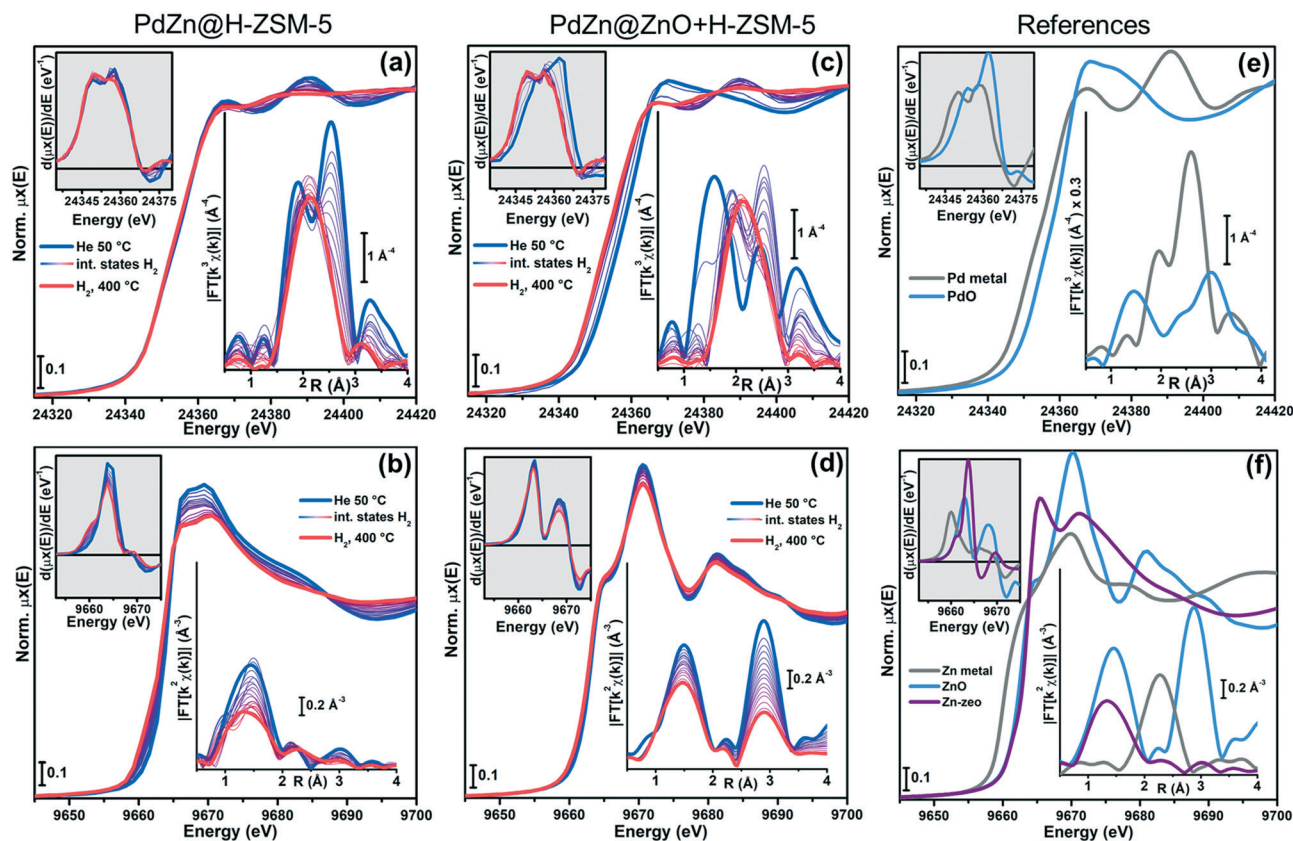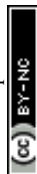This journal is © The Royal Society of Chemistry 2020

Fig. 5 Overview of operando XAS data collected during the activation of the investigated catalysts, carried out in H_2 gas flow, from 50 °C to 400 °C. (a and c) Pd K-edge XANES (main panel) and FT-EXAFS (bottom inset) spectra for (a) PdZn@H-ZSM-5 (25) and (c) PdZn@ZnO + H-ZSM-5 (40). The top insets report the first derivative of the XANES spectra. (b and d) As parts (a and c) but reporting Zn K-edge XAS data for the two catalysts. (e) Pd K-edge XAS data on selected Pd-containing model compounds, namely Pd metal and PdO. (f) Zn K-edge XAS data on selected Zn-containing model compounds, namely Zn metal, ZnO, Zn-exchanged H-ZSM-5 zeolite (1% wt Zn; Si/Al = 40, pretreated in air at 400 °C, from ref. 48). For both catalysts, the reported Pd K-edge FT-EXAFS spectra were obtained by transforming the $k^3\chi(k)$ functions in the 3.0–9.5 Å^{-1} range, while Zn K-edge FT-EXAFS spectra were obtained by transforming the $k^2\chi(k)$ functions in the 2.4–9.5 Å^{-1} range.

zeolites.[48] Throughout the whole activation process, Zn-speciation appears dominated by isolated Zn^{II} ions, without detectable contributions from ZnO. The decrease in the XANES white line peak, as well as in the first-shell maximum observed at *ca.* 1.5 Å in the phase-uncorrected FT-EXAFS spectra suggest a progressive coordination decrease in the first coordination sphere of Zn^{II} ions, possibly connected with the progressive dehydration of Zn^{II} species and their coordination to framework oxygen atoms at zeolite exchange sites. Consistently, the Zn K-edge XANES and EXAFS spectra of PdZn@H-ZSM-5 (25) at the end of the activation in H_2 resembles the ones of a representative dehydrated Zn-exchanged H-ZSM-5, reported in Fig. 5f. All these evidences consistently indicate that a substantial fraction of Zn ions has exchanged into the zeolite component of the bi-functional catalysts, already prior to the activation. Notably, from Zn K-edge XANES of PdZn@H-ZSM-5 (25), a minor contribution from metallic Zn is also observed, in line with the Zn:Pd ratio of ∼5 in the catalyst. In particular, looking at the first derivative XANES spectra in the top inset of Fig. 5b, a feature at *ca.* 9960 eV is noted to progressively develop as temperature increases during the activation, which matches the edge energy position of metallic Zn (Fig. 5f, top inset). This

minor, but still detectable contribution from Zn^0 is expected to come from the Zn atoms participating into the PdZn alloy.

Zn K-edge XAS data obtained for PdZn@ZnO + H-ZSM-5 (40) during the activation (Fig. 5d) clearly show that, in this catalyst, ZnO oxide dominates. This is not surprising, since in this case ZnO represents the support for the PdZn alloy formed upon activation, with an overall Zn:Pd ratio of ∼ 16. Due to the largely dominant ZnO contribution and the bulk averaging nature of the XAS techniques, Zn K-edge XAS in this case is not informative on possible ion-exchange phenomena of Zn ions inside the zeolite component upon activation in H_2. Also, it is not possible to identify the tiny fraction of Zn atoms participating in the PdZn alloy (evident from Pd K-edge XAS results) solely looking at the XANES spectra or even at their first derivatives. However, the differential XANES spectra obtained by calculating the difference between the XANES of PdZn@ZnO + H-ZSM-5 (40) after and before the activation shows a signal structure very similar to the reference differential XANES obtained by subtracting the spectrum of metal Zn from the one of ZnO (Fig. S7†). This observation supports reduction to Zn^0 and alloying with Pd of a very minor fraction of the total Zn

This journal is © The Royal Society of Chemistry 2020

Catal. Sci. Technol., 2020, **10**, 4373–4385 | **4379**

atoms in the system, in line with the compositional characteristics of the catalyst.

After having investigated by XAS the activation process and the final state reached at 400 °C in H_2, we also monitored the two catalysts under reaction conditions at 8 bar, the maximum pressure safely achievable with our gas flow setup. Under these conditions, we have obtained Pd K-edge XAS data, since this absorption edge enables direct structural/electronic sensitivity to the PdZn alloy. The obtained results for the two investigated catalysts monitored during CO_2 hydrogenation at the three temperatures evaluated during the catalytic tests, namely 250, 300 and 350 °C; the spectra collected on the activated catalysts just prior to the reaction at 250 °C in He are also shown for comparison (see ESI,† Fig. S8). Overall, XAS indicates that the formed PdZn alloy remains stable under the reaction feed in both the studied catalysts, with no evidences of important structural modifications or formation of extra-phases. While the XANES is substantially unchanged as a function of the temperature, not surprisingly the EXAFS spectra present a progressive intensity as temperature increases, due to larger thermal contributions to the Debye-Waller factors. It is however interesting to note that, for each probed temperature, the main peak amplitude in the FT-EXAFS of PdZn@H-ZSM-5 (25) is slightly lower than in PdZn@ZnO + H-ZSM-5 (40), suggesting a higher level of structural disorder and/or an average smaller particle size in the former catalyst in agreement with the TEM results.

Fig. 6 reports an overview of the PXRD results at the various stages of the catalyst treatment. In particular, right after H_2 pre-treatment at 400 °C, we observed new peaks around 41.3 and 44.2 °C, compatible with tetragonal β1 PdZn phase.[47,56] The peak intensities slightly increased and their positions slightly shifted with temperature in both catalysts. The PdZn@H-ZSM-5 (25) showed more disordered reflections compared to the PdZn@ZnO + H-ZSM-5 (40) probably due to

smaller crystallite sizes as the TEM and XAS measurements also revealed similar trend in particle size distribution.

Rietveld refinement of PXRD data obtained for PdZn@ZnO + H-ZSM-5 (40) showed that the initial structure of the PdZn@ZnO + H-ZSM-5 contained orthorhombic ZSM-5 phase (*ca.* 90%) and hexagonal ZnO (*ca.* 10%). The atomic parameters of ZSM-5 were fixed to those reported by Schmidt *et al.*[57] which already gave good agreement with experimental pattern. For ZnO phase, isotropic displacement parameters (U_{iso}) of both Zn and O atoms were refined while atomic positions and occupancies were kept fixed. For both structures, unit cell parameters were refined together with profile shape parameters of the Gaussian and Lorentzian components (GW and LY) of the pseudo-Voigt function. Both profile shape parameters were found very similar for the two phases, which indicates that the dominant contribution to the peak broadening is given by the experimental factors (mainly by 2.5 mm thickness of the capillary). Therefore, the profile parameters of the two phases were constrained to be equal in the final refinement. The background was fitted by 5-parameter Legendre polynomial. The final refinement with two phases is shown in the ESI,† Fig. S9, and the obtained structural parameters are reported in Table 3.

Based on the peaks at 41.3° and 44.2°, we then refined the unit cell parameters of the tetragonal PdZn phase and U_{iso} parameter of Pd atom, fixing U_{iso} of Zn to 0, and keeping the atomic coordinates and occupancies fixed. LY and GW profile parameters were fixed to those of H-ZSM-5 and ZnO phases, while additional LX contribution was added to account for the size effects. The crystallite size was then calculated as $D = \frac{36000\lambda}{\pi^2 LX} = 26 \pm 1$ nm. This number is in the upper limit of the values found by TEM investigations in section 3.1 (and ESI† Fig. S3). This can be explained by (i) the stronger contribution of bigger particles to PXRD signal (see green bars in part b of Fig. S3 I†), (ii) the possible overestimation of experimental contribution (GW and LY) and (iii) the presence of both Pd and Pd–Zn particles in the TEM images, while the PXRD only considered the tetragonal PdZn phase. The results of the refinement and the obtained structural parameters are reported in Table 3. Particularly, the fraction of ZnO phase
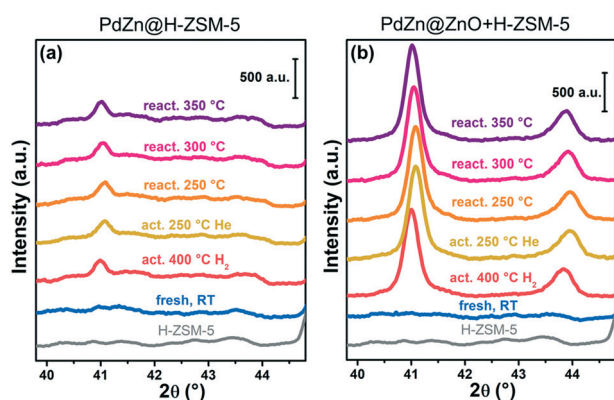

Fig. 6 PXRD patterns collected, quasi simultaneously to XAS spectra, at key conditions for (a) PdZn@H-ZSM-5 (25) and (b) PdZn@ZnO + H-ZSM-5 (40), reported in the 2θ range where the characteristic reflections of the PdZn alloy occur. The PXRD pattern of pure H-ZSM-5 zeolite is also reported for comparison. The patterns are vertically translated for clarity.

Table 3 Results of Rietveld refinement of PdZn@ZnO + H-ZSM-5 (40)

Phase	Refined parameter	Initial	After activation	Spent
H-ZSM-5	Fraction, %	89.9(7)	89.4(9)	90.2(8)
	a, Å	20.101(1)	20.075(1)	20.087(1)
	b, Å	19.915(1)	19.920(1)	19.914(1)
	c, Å	13.4002(9)	13.3939(9)	13.3984(9)
ZnO	Fraction, %	10.1(7)	9.8(7)	8.9(6)
	a, Å	3.25076(8)	3.25940(9)	3.2510(1)
	b, Å	5.2075(2)	5.2166(2)	5.2079(2)
	c, Å	0.0100(4)	0.0184(4)	0.0096(4)
PdZn	Fraction, %	—	0.79(2)	0.85(2)
	a, Å	—	4.1262(5)	4.1005(3)
	c, Å	—	3.3463(7)	3.3373(4)
	U_{iso}(Pd), Å^2	—	0.036(5)	0.023(3)

4380 | *Catal. Sci. Technol.*, 2020, **10**, 4373–4385

This journal is © The Royal Society of Chemistry 2020

decreases, indicating that Zn atoms may be transferred either to Zn–Pd alloy nanoparticles or to the zeolite framework.

3.4 Hydrogenation of CO_2

Fig. 7(a)–(c) shows the CO_2 catalytic hydrogenation *versus* TOS over the various catalysts at 300 °C and 20 bar. Focusing first on PdZn@ZnO alone (without H-ZSM-5), it initially yielded 17% CO_2 conversion, that decreased to 11.6% over 20 h (Fig. 7(a)). Selectivity to MeOH sharply increased from 0 to 32% with corresponding decrease in CO selectivity from 92% to 65% during the first 6 h, and then the MeOH and CO selectivities gradually merged at appx. 50% selectivity by 20 h TOS, possibly due to delay in the formation of the active site for MeOH. Fig. 7(d) and Fig. 8(a) show that the space time yield (STY) of MeOH over PdZn@ZnO increased with temperature from 250 to 300 °C, and that the yield of MeOH (5.5%) approached the thermodynamic equilibrium yield of 5.9% after 20 h on stream at 300 °C. This result is superior to a previous report devoted to PdZn on ZnO support: In that study, the MeOH yield decreased from 6.4% at 250 °C to 4.2% at 300 °C, with a space time yield of 1.6 mol kg^{-1} h^{-1} at 300 °C (see Fig. 2, It should be noted that the sample was made by sol-immobilization method, and tested at 3600 ml/g h WHSV in a 0.5 × 50 cm^2 stainless tube reactor).[7] A further temperature increase to 350 °C led to dramatically lower MeOH STY and selectivity over the PdZn@ZnO catalyst (Fig. 7). Comparison to the thermodynamic equilibrium value (Fig. 8) showed that the system was farther from equilibrium at this temperature than at 300 °C, suggesting that the
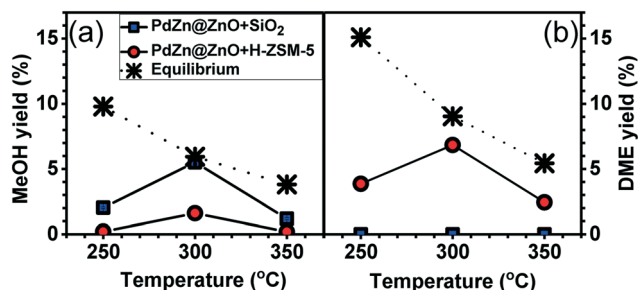

Fig. 8 Comparison of oxygenate ((a) MeOH and (b) DME) yields from the CO_2 hydrogenation reaction at 20 bar with theoretical equilibrium yields *versus* temperature.

system deactivated further when reaching the higher temperature.

The second case examined in our tests was the physically mixed H-ZSM-5 (40) and PdZn@ZnO in 1 : 1 ratio (Fig. 7b). Here, the CO_2 conversion was 20% and slightly decreased to 17% after 11 h TOS at 300 °C. Aside the CO and MeOH main products, high amounts of DME were observed with minor amounts of methane and C_{2+} hydrocarbons (accounting for <2% overall). The selectivity to oxygenates (DME and MeOH) gradually increased from 35 to 52% over 11 h TOS at the expense of CO. Notably, beyond 11 h, conversion and selectivity reached a steady state that was maintained up to the 45 h TOS studied (only the first 30 h is shown here for brevity). Generally, the addition of H-ZSM-5 to the PdZn@ZnO catalysts shifted the oxygenates yield beyond MeOH thermodynamic equilibrium yield, in agreement with
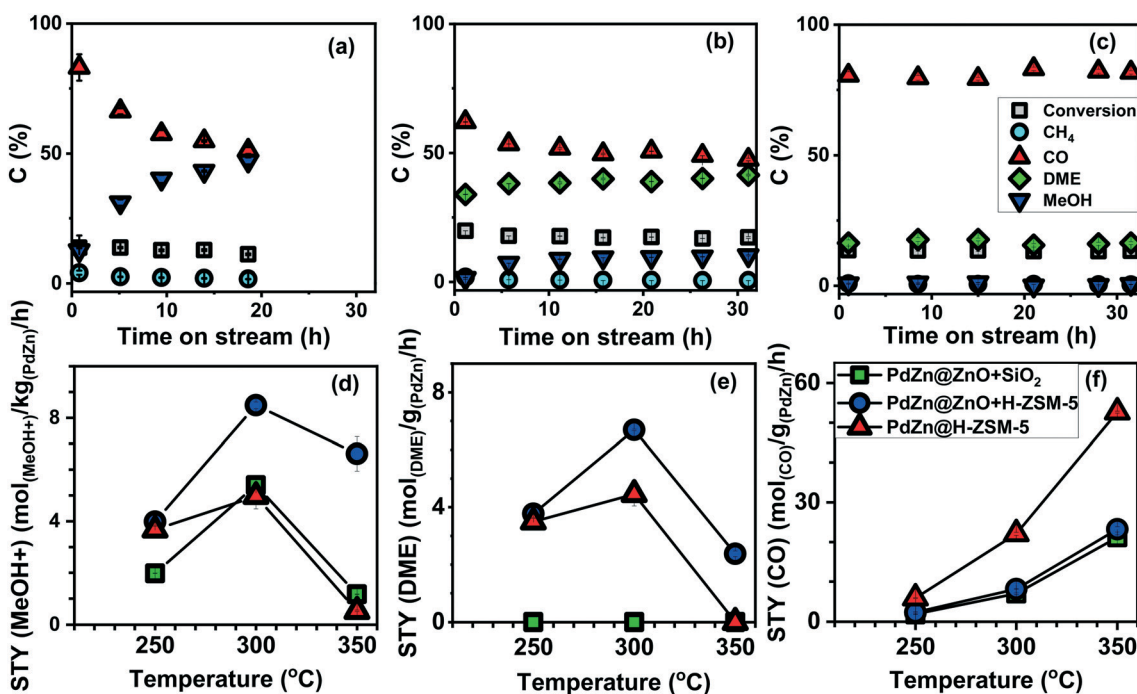

Fig. 7 Conversion and selectivity *versus* time on stream at 300 °C over (a) PdZn@ZnO + SiO$_2$, (b) PdZn@ZnO + H-ZSM-5, (c) PdZn@H-ZSM-5. Space time yield (STY) comparison of the catalysts *versus* temperature for the formation of (d) MeOH+ (sum of MeOH, DME and C$_{2+}$ hydrocarbons), (e) DME, (f) CO, the catalysts were pretreated in H$_2$ flow at 400 °C and tested at 20 bar with H$_2$/CO$_2$ = 3, and WHSV = 6000 ml g^{-1} h^{-1}.

This journal is © The Royal Society of Chemistry 2020

Catal. Sci. Technol., 2020, **10**, 4373–4385 | **4381**

literature reports,[36] since further conversion of MeOH to DME or hydrocarbons is more thermodynamically favourable than ending the reaction at MeOH as illustrated in Fig. 1. Overall, we observed 8.8% yield to the oxygenates at 300 °C, very close to the 9% estimated DME equilibrium yield (see Fig. 8), and surpassing the previously reported 4.2% oxygenates yield at the same temperature and pressure.[36] Increasing the temperature to 350 °C, a substantial decrease was observed in MeOH and DME STY and yields, the oxygenate yield now being further away from equilibrium than at 300 °C. This result is in agreement with that observed over PdZn@ZnO alone, and suggests that similar deactivation of the MeOH forming active sites takes place with and without the physical mixture with H-ZSM-5. Turning next our attention to the CO space time yield over these two catalysts (Fig. 7(f)), it increases exponentially with temperature, and is the same for both catalysts. This result suggests that the CO forming active sites are also not influenced by mixing the two catalysts.

The third case consisting of PdZn grafted on H-ZSM-5 is shown in Fig. 7c. CO_2 conversion remained at 13%, with 81 and 17% selectivity to CO and DME respectively, at 300 °C. Meanwhile, selectivities to MeOH and C_{2+} accounted for less than 2% over the 33 h TOS studied. Here, the conversions and selectivities were relatively stable compared to that of PdZn@ZnO + H-ZSM-5 (40) at least within the first 10 h TOS. However, clearly the physical mixture outperformed the grafted catalysts both in terms of yield and selectivity to the oxygenates at 300 °C. Next, we turn to compare the space time yield (STY) for the formation of DME, MeOH+ (sum of MeOH, DME and C_{2+} hydrocarbons) and CO at 250–350 °C over the three catalysts (Fig. 7(d)–(f)). As reported above, PdZn@ZnO showed no DME formation at all temperatures, however, the inclusion of H-ZSM-5 either by grafting or physical mixing induced high activity towards DME formation. STY for DME and MeOH+ increased up to 300 °C and then declined with temperature. Maxima of 6.7 and 4.5 $mol_{(DME)}$ $kg_{(PdZn)}^{-1}$ h^{-1} DME STY were observed at 300 °C for the PdZn@ZnO + H-ZSM-5 (40) and PdZn@H-ZSM-5 (25) respectively. Similarly, for MeOH+, the optimal STY measured at 300 °C were 5.4, 8.5 and 4.9 $mol_{(MeOH+)}$ $kg_{(PdZn)}^{-1}$ h^{-1} for the PdZn@ZnO, PdZn@ZnO + H-ZSM-5 (40) and PdZn@H-ZSM-5 (25) respectively. STY for CO increased with temperature over all catalysts, but more rapidly for the PdZn@H-ZSM-5 compared to that of the PdZn@ZnO and PdZn@ZnO + H-ZSM-5.

4. Discussion

The characterization data from XAS, PXRD and TEM, of the investigated hybrid PdZn/zeolite catalysts for CO_2 conversion, consistently showed that upon H_2 pre-treatment, Pd-Zn alloy was gradually formed from *ca.* 300 °C upward. The XAS data of the as-prepared PdZn@H-ZSM-5 already showed the Pd^0 characteristic features, whilst the PdZn@ZnO + H-ZSM-5 still had substantial amount of Pd^{II} in its as-prepared state. Upon

H_2 treatment with temperature, the Pd K-edge XAS showed the characteristic features of PdZn alloy in both hybrid materials. In parallel, PXRD also showed the emergence of new peaks at 41.3° and 44.2° denoting the formation of tetragonal β1 PdZn alloy nanoparticles. PdZn@H-ZSM-5 exhibited a much higher level of structural disorder compared to the PdZn@ZnO + H-ZSM-5, as evidenced by very weak and broadened peaks in its PXRD patterns, which hampered Rietveld refinement of these data. The TEM showed the presence of the PdZn alloy with different particle sizes, smaller in the case of the PdZn@ZSM-5 compared to the PdZn@ZnO+H-ZSM-5, consistent with indications from PXRD.

Regarding catalytic testing results, conversions were generally stable or slightly decreased over time. However, there was always some delay in attaining steady selectivity to products despite pre-treatment in H_2 at 400 °C for all the catalysts prior to testing. The PdZn@H-ZSM-5 catalyst attained a stable selectivity much earlier than the PdZn@ZnO + SiO_2 or PdZn@ZnO + H-ZSM-5 samples. On a similar line, the XAS data showed that the PdZn@H-ZSM-5 catalyst developed the PdZn alloy characteristic feature earlier than PdZn@ZnO + H-ZSM-5 during thermal activation in H_2. Even though in the final state after activation, the two catalysts showed similar XAS characteristic of Pd^0 sites in bimetallic PdZn, it is possible that attaining full formation of the Pd–Zn alloy took longer time in the macroscale catalytic testing setup compared to the capillary reactor cell used for the operando XAS, due to the smaller amount of sample used in the latter case. Thus, the delay in the attaining steady selectivity can be related to longer time in forming the active PdZn site.

The activity in the different combinations of catalyst differed. Firstly, comparing the PdZn@ZnO with and without H-ZSM-5, the presence of H-ZSM-5 led to higher activity towards oxygenates. Here, there is a clear promotion of MeOH+ especially at higher temperatures (>300 °C), where the conversion of MeOH to DME or hydrocarbons becomes important.[43,44] Interestingly, the STYs of CO were similar over both catalysts at the different temperatures. It has been reported[30] that COOH intermediate which decompose to CO (and H_2O) is better stabilized on Pd(111) surface rather than HCOO intermediate which hydrogenates to MeOH on PdZn surface. Therefore, this report is in agreement with our observations and suggest that given the same reaction conditions, MeOH and CO formations occur at distinct active sites, such that the presence of H-ZSM-5 only increased oxygenates formation without any influence on CO formation.

Beyond this, the catalyst produced by SOMC, PdZn@H-ZSM-5 (25) showed rather high yield of CO compared to the PdZn@ZnO + H-ZSM-5 (40). Nonetheless, the PdZn active sites were relatively similar in both catalysts except for the particle size, which was even smaller in the PdZn@H-ZSM-5 (25). Even though there were differences in the Si/Al ratio of the H-ZSM-5, this is not expected to influence CO_2 conversion

4382 | *Catal. Sci. Technol.*, 2020, **10**, 4373–4385

This journal is © The Royal Society of Chemistry 2020

to MeOH. One main difference however on the side of CO_2 to MeOH catalyst, is the Zn/Pd ratio in the two hybrid systems. It has already been reported that having neighbouring Zn^0 around Pd atom significantly suppresses *trans*-COOH which leads to RWGS reaction.[6] Therefore, the enhanced oxygenates formation in the PdZn@ZnO + H-ZSM-5 can be attributed to the presence of a higher amount of Zn neighbours around Pd atom.

Despite the requirement of adequate supply of neighbouring Zn atoms around Pd atom, it appears it comes at a cost. In the hybrid catalyst systems, considerable amount of DME were observed rather than the expected hydrocarbons.[58] DME formation is known to precede hydrocarbon formation in MTH reactions *via* MeOH dehydration over Brønsted acid sites.[59,60] MeOH dehydration is mechanistically suggested to occur over the acid sites *via* either associative route, which involves protonated MeOH dimer formation, or dissociative route involving methoxy reacting with MeOH. Higher MeOH pressures favours dimer formation whilst dissociation of proton from MeOH is less favoured. Furthermore MTH reaction is known to involve an induction period due to initial C–C bond formation, hydrocarbon pool and autocatalytic reactions,[61] more pronounced at lower temperatures.[62] The induction period significantly reduces with increasing temperature, as it has been reported for example that the induction period reduced from 120 to 10 min at 260 and 280 °C respectively with about 25 to 37% MeOH conversion to hydrocarbons over H-ZSM-5 with 4 g_{MeOH} $g_{H-ZMS-5}^{-1}$ h^{-1} WHSVs.[62] Hence, considering the rather low WHSV (*i.e.* 0.27 and 0.21 g_{MeOH} $g_{H-ZMS-5}^{-1}$ h^{-1}, based on amount of oxygenates produced over PdZn@ZnO + H-ZSM-5 (40) in this study respectively) at 300 and 350 °C, the reaction was expected to proceed beyond DME to hydrocarbons.

One important factor in the MTH mechanism is the presence of Brønsted acid sites.[63] The XAS data showed that the Zn K-edge spectrum of PdZn@H-ZSM-5 was dominated by Zn^{II} ions which progressively decrease in coordination during pre-treatment (activation) and closely resembled dehydrated Zn-exchanged H-ZSM-5.[48] Even though in the Zn K-edge XAS spectrum of PdZn@ZnO + H-ZSM-5 (40), Zn^{II} ion migration evidence was overshadowed by the dominant response from ZnO support, we can infer from the PdZn@H-ZSM-5 (40) results that a substantial fraction of Zn ions has exchanged into the zeolite component of the bi-functional catalysts. The FT-IR data indicated a substantial decrease in the Brønsted acid site for the PdZn@H-ZSM-5 and PdZn@ZnO + H-ZSM-5 prior to the reaction feed as well as the spent hybrid catalyst whilst the amount of Lewis acid sites increased. This suggested that the Zn^{II} ion-exchanged with the protons in the zeolite to poison their Brønsted acid sites. As a result, the Brønsted acid required to initiate hydrocarbon formation from MeOH or DME was inadequate, which explains why the MeOH conversion ended in DME formation.

As a final note, the observation of concurrent ZnO reduction to form PdZn alloy nanoparticles, and Zn^{2+} diffusion followed by ion exchange with H^+ in the zeolite, both during pretreatment in a H_2 flow, may seem contradictory. To this end, it is important to note that the Gibbs free energy of Zn oxidation (eqn (5)) is −358 kJ mol^{-1} at 400 °C, corresponding to an equilibrium constant of 6.5 × 10^{27}. Hence, minor traces of O_2 (or H_2O) in the gas will stabilize zinc in the Zn^{2+} state, as experimentally demonstrated by Lew *et al.*[64]

$$Zn + 0.5O_2 \rightleftharpoons ZnO \qquad (5)$$

Considering next the formation of PdZn alloy phase, Kou and Chang reported high stability of intermetallic phases formed between Zn and group VIII transition metals such as Pd.[65] They ascribed the stabilization to transfer of electrons from Zn to the d-band of Pd, thus suggesting that Pd co-presence impacts ZnO reduction.

5. Conclusion

CO_2 hydrogenation to DME was performed over PdZn alloy mixed with H-ZSM-5 catalyst. Although two different methods (SOMC grafting and physical mixture) were employed to introduce the Pd–Zn on the zeolite, operando PXRD and XAS showed that similar active sites (PdZn alloy) were generated in both cases prior to CO_2 hydrogenation reaction feed conditions. Furthermore, PdZn alloy which is the active site for MeOH synthesis remained stable under reaction conditions within the 250–350 °C temperature range with no important structural modifications or extra-phases formed except crystallite size growth. Physical mixture of PdZn@ZnO with H-ZSM-5 showed an enhanced oxygenates yield of 8.8% at 300 °C, which approached thermodynamic equilibrium yield of DME but beyond that of MeOH. With ZnO as support, PdZn@ZnO + H-ZSM-5 performed better than PdZn grafted on H-ZSM-5 by SOMC, attributed to higher amount of Zn which suppressed isolated Pd atoms. Instead of hydrocarbons, DME was rather observed in the hybrid catalysts. Clearly, this was due to Zn ion migration into the zeolite thereby poisoning the Brønsted acid sites responsible for hydrocarbon formation. Overall, even though increased number of neighbouring Zn^0 is required to optimize the PdZn alloy formation, excess Zn have the tendency to diffuse into the zeolite to replace acid protons rendering it less effective for hydrocarbon formation.

Cascade reactions over hybrid catalysts represent a promising approach in designing more effective routes to convert CO_2 into value-added products. However, the presented results for PdZn/zeolite hybrid catalysts exemplify how the different functionalities could undertake unexpected interactions, ultimately biasing the hybrid catalyst performance. In this context, a careful and balanced choice of the compositional characteristics, together with detailed characterization under reaction-relevant conditions, are crucial to design improved multi-functional catalytic systems for CO_2 valorisation.

This journal is © The Royal Society of Chemistry 2020

Catal. Sci. Technol., 2020, **10**, 4373–4385 | **4383**

Conflicts of interest

"There are no conflicts to declare".

Acknowledgements

References

1 H. Yang, C. Zhang, P. Gao, H. Wang, X. Li, L. Zhong, W. Wei and Y. Sun, *Catal. Sci. Technol.*, 2017, **7**, 4580–4598.

2 G. A. Florides and P. Christodoulides, *Environ. Int.*, 2009, **35**, 390–401.

3 World Energy agency, Overview and key findings.

4 W. J. Thomas and S. Portalski, *Ind. Eng. Chem.*, 1958, **50**, 967–970.

5 J. B. Hansen and P. E. Højlund Nielsen, in *Handbook of Heterogeneous Catalysis*, ed. G. Ertl, H. Knözinger, F. Schüth, J. Weitkamp, H. G. Karge and H. Pfeifer, Wiley-VCH Verlag GmbH & Co. KGaA, Weinheim, Germany, 2008, pp. 2920–2949.

6 F. Liao, X.-P. Wu, J. Zheng, M. M.-J. Li, A. Kroner, Z. Zeng, X. Hong, Y. Yuan, X.-Q. Gong and S. C. E. Tsang, *Green Chem.*, 2017, **19**, 270–280.

7 H. Bahruji, M. Bowker, G. Hutchings, N. Dimitratos, P. Wells, E. Gibson, W. Jones, C. Brookes, D. Morgan and G. Lalev, *J. Catal.*, 2016, **343**, 133–146.

8 H. Bahruji, M. Bowker, W. Jones, J. Hayward, J. Ruiz Esquius, D. J. Morgan and G. J. Hutchings, *Faraday Discuss.*, 2017, **197**, 309–324.

9 J. Xu, X. Su, X. Liu, X. Pan, G. Pei, Y. Huang, X. Wang, T. Zhang and H. Geng, *Appl. Catal., A*, 2016, **514**, 51–59.

10 C.-H. Kim, J. S. Lee and D. L. Trimm, *Top. Catal.*, 2003, **22**, 319–324.

11 A. S. Malik, S. F. Zaman, A. A. Al-Zahrani, M. A. Daous, H. Driss and L. A. Petrov, *Appl. Catal., A*, 2018, **560**, 42–53.

12 A. Ota, E. L. Kunkes, I. Kasatkin, E. Groppo, D. Ferri, B. Poceiro, R. M. Navarro Yerga and M. Behrens, *J. Catal.*, 2012, **293**, 27–38.

13 S. Bai, Q. Shao, P. Wang, Q. Dai, X. Wang and X. Huang, *J. Am. Chem. Soc.*, 2017, **139**, 6827–6830.

14 A. García-Trenco, E. R. White, A. Regoutz, D. J. Payne, M. S. P. Shaffer and C. K. Williams, *ACS Catal.*, 2017, **7**, 1186–1196.

15 S. E. Collins, J. J. Delgado, C. Mira, J. J. Calvino, S. Bernal, D. L. Chiavassa, M. A. Baltanás and A. L. Bonivardi, *J. Catal.*, 2012, **292**, 90–98.

16 E. M. Fiordaliso, I. Sharafutdinov, H. W. P. Carvalho, J.-D. Grunwaldt, T. W. Hansen, I. Chorkendorff, J. B. Wagner and C. D. Damsgaard, *ACS Catal.*, 2015, **5**, 5827–5836.

17 K. Sun, Z. Fan, J. Ye, J. Yan, Q. Ge, Y. Li, W. He, W. Yang and C.-j. Liu, *J. CO2 Util.*, 2015, **12**, 1–6.

18 O. Martin, A. J. Martín, C. Mondelli, S. Mitchell, T. F. Segawa, R. Hauert, C. Drouilly, D. Curulla-Ferré and J. Pérez-Ramírez, *Angew. Chem., Int. Ed.*, 2016, **55**, 6261–6265.

19 P. Gao, S. Li, X. Bu, S. Dang, Z. Liu, H. Wang, L. Zhong, M. Qiu, C. Yang, J. Cai, W. Wei and Y. Sun, *Nat. Chem.*, 2017, **9**, 1019.

20 J. Gao, C. Jia and B. Liu, *Catal. Sci. Technol.*, 2017, **7**, 5602–5607.

21 J. L. Snider, V. Streibel, M. A. Hubert, T. S. Choksi, E. Valle, D. C. Upham, J. Schumann, M. S. Duyar, A. Gallo, F. Abild-Pedersen and T. F. Jaramillo, *ACS Catal.*, 2019, **9**, 3399–3412.

22 N. Akkharaphatthawon, N. Chanlek, C. K. Cheng, M. Chareonpanich, J. Limtrakul and T. Witoon, *Appl. Surf. Sci.*, 2019, **489**, 278–286.

23 J. Wang, G. Li, Z. Li, C. Tang, Z. Feng, H. An, H. Liu, T. Liu and C. Li, *Sci. Adv.*, 2017, **3**, e1701290.

24 R. Raudaskoski, M. V. Niemelä and R. L. Keiski, *Top. Catal.*, 2007, **45**, 57–60.

25 J. Liu, J. Shi, D. He, Q. Zhang, X. Wu, Y. Liang and Q. Zhu, *Appl. Catal., A*, 2001, **218**, 113–119.

26 X.-M. Liu, G. Q. Lu and Z.-F. Yan, *Appl. Catal., A*, 2005, **279**, 241–245.

27 J. Słoczyński, R. Grabowski, A. Kozłowska, P. Olszewski, J. Stoch, J. Skrzypek and M. Lachowska, *Appl. Catal., A*, 2004, **278**, 11–23.

28 J. Słoczyński, R. Grabowski, P. Olszewski, A. Kozłowska, J. Stoch, M. Lachowska and J. Skrzypek, *Appl. Catal., A*, 2006, **310**, 127–137.

29 T. Phongamwong, U. Chantaprasertporn, T. Witoon, T. Numpilai, Y. Poo-arporn, W. Limphirat, W. Donphai, P. Dittanet, M. Chareonpanich and J. Limtrakul, *Chem. Eng. J.*, 2017, **316**, 692–703.

30 F. Liao, X.-P. Wu, J. Zheng, M.-J. Li, Z. Zeng, X. Hong, A. Kroner, Y. Yuan, X.-Q. Gong and S. C. E. Tsang, *Catal. Sci. Technol.*, 2016, **6**, 7698–7702.

31 T. A. Semelsberger, R. L. Borup and H. L. Greene, *J. Power Sources*, 2006, **156**, 497–511.

32 G. J. Hutchings and R. Hunter, *Catal. Today*, 1990, **6**, 279–306.

33 J. S. Martinez-Espin, M. Mortén, T. V. W. Janssens, S. Svelle, P. Beato and U. Olsbye, *Catal. Sci. Technol.*, 2017, **7**, 2700–2716.

4384 | *Catal. Sci. Technol.*, 2020, **10**, 4373–4385

This journal is © The Royal Society of Chemistry 2020

34 T. Witoon, T. Permsirivanich, N. Kanjanasoontorn, C. Akkaraphataworn, A. Seubsai, K. Faungnawakij, C. Warakulwit, M. Chareonpanich and J. Limtrakul, *Catal. Sci. Technol.*, 2015, **5**, 2347–2357.

35 Y. Suwannapichat, T. Numpilai, N. Chanlek, K. Faungnawakij, M. Chareonpanich, J. Limtrakul and T. Witoon, *Energy Convers. Manage.*, 2018, **159**, 20–29.

36 H. Bahruji, R. D. Armstrong, J. Ruiz Esquius, W. Jones, M. Bowker and G. J. Hutchings, *Ind. Eng. Chem. Res.*, 2018, **57**, 6821–6829.

37 G. Bonura, M. Cordaro, L. Spadaro, C. Cannilla, F. Arena and F. Frusteri, *Appl. Catal., A*, 2013, **140-141**, 16–24.

38 G. Bonura, M. Migliori, L. Frusteri, C. Cannilla, E. Catizzone, G. Giordano and F. Frusteri, *J. CO2 Util.*, 2018, **24**, 398–406.

39 H. Nakamoto and H. Takahashi, *Zeolites*, 1982, **2**, 67–68.

40 E. Catizzone, A. Aloise, M. Migliori and G. Giordano, *Appl. Catal., A*, 2015, **502**, 215–220.

41 S. Jiang, J.-S. Hwang, T.-H. Jin, T. Cai, W. Cho, Y.-S. Baek and S.-E. Park, *Bull. Korean Chem. Soc.*, 2004, **25**, 185–189.

42 T. Sakakura, J.-C. Choi and H. Yasuda, *Chem. Rev.*, 2007, **107**, 2365–2387.

43 F. Bleken, M. Bjørgen, L. Palumbo, S. Bordiga, S. Svelle, K.-P. Lillerud and U. Olsbye, *Top. Catal.*, 2009, **52**, 218–228.

44 H. Schulz, Z. Siwei and H. Kusterer, in *Studies in Surface Science and Catalysis*, ed. T. Inui, S. Namba and T. Tatsumi, Elsevier, 1991, vol. 60, pp. 281–290.

45 P. Rouge, A. Garron, S. Norsic, C. Larabi, N. Merle, L. Delevoye, R. M. Gauvin, K. C. Szeto and M. Taoufik, *Mol. Catal.*, 2019, **471**, 21–26.

46 K. C. Szeto, A. Gallo, S. Hernández-Morejudo, U. Olsbye, A. De Mallmann, F. Lefebvre, R. M. Gauvin, L. Delevoye, S. L. Scott and M. Taoufik, *J. Phys. Chem. C*, 2015, **119**, 26611–26619.

47 M. W. Tew, H. Emerich and J. A. van Bokhoven, *J. Phys. Chem. C*, 2011, **115**, 8457–8465.

48 I. Pinilla-Herrero, E. Borfecchia, J. Holzinger, U. V. Mentzel, F. Joensen, K. A. Lomachenko, S. Bordiga, C. Lamberti, G. Berlier, U. Olsbye, S. Svelle, J. Skibsted and P. Beato, *J. Catal.*, 2018, **362**, 146–163.

49 E. Selli and L. Forni, *Microporous Mesoporous Mater.*, 1999, **31**, 129–140.

50 W. van Beek, O. V. Safonova, G. Wiker and H. Emerich, *Phase Transitions*, 2011, **84**, 726–732.

51 B. Ravel and M. Newville, *J. Synchrotron Radiat.*, 2005, **12**, 537–541.

52 J. Kieffer and J. P. Wright, *Powder Diffr.*, 2013, **28**, S339–S350.

53 A. Hammersley, *J. Appl. Crystallogr.*, 2016, **49**, 646–652.

54 M. Gentzen, D. E. Doronkin, T. L. Sheppard, A. Zimina, H. Li, J. Jelic, F. Studt, J.-D. Grunwaldt, J. Sauer and S. Behrens, *Angew. Chem., Int. Ed.*, 2019, **58**, 15655–15659.

55 J. R. Gallagher, D. J. Childers, H. Zhao, R. E. Winans, R. J. Meyer and J. T. Miller, *Phys. Chem. Chem. Phys.*, 2015, **17**, 28144–28153.

56 E. J. Peterson, B. Halevi, B. Kiefer, M. N. Spilde, A. K. Datye, J. Peterson, L. Daemen, A. Llobet and H. Nakotte, *J. Alloys Compd.*, 2011, **509**, 1463–1470.

57 W. Schmidt, U. Wilczok, C. Weidenthaler, O. Medenbach, R. Goddard, G. Buth and A. Cepak, *J. Phys. Chem. B*, 2007, **111**, 13538–13543.

58 T. V. W. Janssens, *J. Catal.*, 2009, **264**, 130–137.

59 A. J. Jones and E. Iglesia, *Angew. Chem., Int. Ed.*, 2014, **53**, 12177–12181.

60 A. Ghorbanpour, J. D. Rimer and L. C. Grabow, *ACS Catal.*, 2016, **6**, 2287–2298.

61 U. Olsbye, S. Svelle, K. P. Lillerud, Z. H. Wei, Y. Y. Chen, J. F. Li, J. G. Wang and W. B. Fan, *Chem. Soc. Rev.*, 2015, **44**, 7155–7176.

62 L. Qi, Y. Wei, L. Xu and Z. Liu, *ACS Catal.*, 2015, **5**, 3973–3982.

63 L. Qi, J. Li, Y. Wei, Y. He, L. Xu and Z. Liu, *RSC Adv.*, 2016, **6**, 52284–52291.

64 S. Lew, A. F. Sarofim and M. Flytzani-Stephanopoulos, *Chem. Eng. Sci.*, 1992, **47**, 1421–1431.

65 S. Kou and Y. A. Chang, *Acta Metall.*, 1975, **23**, 1185–1190.

This journal is © The Royal Society of Chemistry 2020

Catal. Sci. Technol., 2020, **10**, 4373–4385 | 4385